*J. Fluid Mech.* (2014), *vol.* 748, *pp.* 221–240. © Cambridge University Press 2014 
doi:10.1017/jfm.2014.144

# Nonlinear and dispersive free surface waves propagating over fluids with weak vertical and horizontal density variation

**Sangyoung Son**[1,2] **and Patrick J. Lynett**[2,†]

[1]Department of Civil and Environmental Engineering, University of Ulsan, Ulsan 680-749, Republic of Korea

[2]Sonny Astani Department of Civil and Environmental Engineering, University of Southern California, Los Angeles, CA 90089, USA

(Received 1 July 2013; revised 15 January 2014; accepted 11 March 2014; first published online 28 April 2014)

We consider the change in fluid density in a depth-integrated long-wave model. By allowing horizontal and vertical variation of fluid density, a depth-integrated model for long gravity waves over a variable-density fluid has been developed, where density change effects are included as correction terms. In particular, a two-layer fluid system is chosen to represent vertical density variations, where interfacial wave effects on the free surface are accounted for through direct inclusion of the velocity component of the interfacial wave. For the numerical implementation of the model, a finite-volume scheme coupled with an approximate Riemann solver is adopted for leading-order terms while cell-centred finite-volume methods are utilized for others. Numerical tests in which the density field is configured to vary either horizontally or vertically have been performed to verify the model. For horizontal variation of fluid density, a pneumatic breakwater system is simulated and fair agreement is observed between computed and measured data, indicating that the current induced by the upward bubble flux is responsible for wave attenuation to some degree. To investigate the effects of internal motion on the free surface, a two-layer fluid system with monochromatic internal wave motion is tested numerically. Simulated results agree well with the measured and analytical data. Lastly, nonlinear interactions between external- and internal-mode surface waves are studied numerically and analytically, and the model is shown to have nonlinear accuracy limitations similar to existing Boussinesq-type models.

**Key words:** internal waves, stratified flows, surface gravity waves

## 1. Introduction

Geophysical flows in variable-density fluids are common in the ocean environment due to thermal or saline gradients. In particular, the flows in estuaries and river mouths exhibit horizontal density variation as well as vertical stratification as freshwater and seawater are exchanged and mixed. The complexity produced by density changes drives other physical mechanisms, which are not expected in constant-density fluids and can affect mass and momentum transport. For instance,

† Email address for correspondence: plynett@usc.edu

https://doi.org/10.1017/jfm.2014.144 Published online by Cambridge University Press

from a dynamical standpoint, for two fluids separated horizontally, an imbalance of hydrostatic pressure between them is expected if they have the same surface level but different densities, and this causes fluid movement (e.g. gravity currents) to cancel out such pressure differences. Two-layer exchange flows through a contraction or classic lock-exchange problems present good examples of this (Wood 1970; Armi & Farmer 1986). From a kinematic standpoint, in contrast, the complexity lies in the fact that less momentum is needed for conveying lighter fluids. Internal waves at a density interface can arise under vertical stratification. If an initial disturbance at the interface is introduced, it will freely propagate as an oscillating wave to maintain a balance between the restoring force (i.e. gravity) and buoyancy. Either the horizontal or the vertical pycnocline is, therefore, of primary concern in estuarine hydrodynamics and a necessary subject for a complete consideration of coastal environments. Many researchers have corresponding interests over several decades in investigating hydrodynamics in variable-density fluids, and recent advances have been made in both numerical and observational studies.

Fluid density inherently exhibits three-dimensional (3D) variations in natural oceanic systems (Mellor 1991), and hence 3D non-hydrostatic models coupled with the density transport equation are commonly adopted for simulation of density-varying fluid flows (e.g. Kanarsk & Maderich 2003). In fact, for practical and scholarly purposes, different physical set-ups of density variations are ideally assumed at the initial state, and hence different features have been highlighted in the literature. For the horizontal variation of density, whose main driving force is the hydrostatic pressure difference (i.e. buoyancy), many studies deal with gravity currents (or buoyancy currents) in lock-exchange configurations with a rigid lid on the upper boundary (e.g. Lowe, Rottman & Linden 2005) or with bidirectional flows of two fluids of different density (e.g. Armi & Farmer 1986). Such studies focus on the internal physics, such as the diffusion and mixing resulting from barotropic forces. Meanwhile, for surface physics, Leighton, Borthwick & Taylor (2010) recently presented a 1D model for vertically well mixed shallow flows with a horizontal density gradient. They established a single-phase model by assuming the vertical variation of fluid density to be negligible; otherwise, a two-phase model is typically adopted.

Unlike horizontal density variations, vertical stratification is often simplified by using two layers, since the case of two-layer fluids having different densities is the norm in estuarine systems. Provided that the fluids remain stably stratified without any motion, there is no driving force due to the stratification. The subject of density stratification, however, broadens the area of the present study to include interfacial physics at the boundary between layers and leads us to consider internal waves, since two-layer systems provide a situation in which interfacial oscillations can travel.

In a two-layer system, the fluid exhibits a sharp density interface between the upper and lower layers, and an interfacial disturbance can be generated by topographical or other forces (e.g. Farmer & Armi 1999; Helfrich & Melville 2006) that may propagate along the interface, influencing the physical process over the entire water body. However, most of the literature on this topic is concerned with the physical properties of the internal wave itself, without considering the free surface wave components. By imposing the rigid-lid assumption on the upper boundary, the relevant physical problem can be simplified so as to allow a focus solely on the internal physics (e.g. Evans & Ford 1996). On the basis of this idea, numerous models have been developed for internal wave propagation over either shallow or deep water (Koop & Butler 1981; Segur & Hammack 1982; Choi & Camassa 1999; Debsarma, Das & Kirby 2010).

https://doi.org/10.1017/jfm.2014.144 Published online by Cambridge University Press

Through theoretical studies (Lamb 1932; Phillips 1977; Hwung, Yang & Shugan 2009) and observations (Elachi & Apel 1976), it has been demonstrated that subsurface movement can affect the free surface. Among the most well-known examples are the surface signature observed by satellite synthetic aperture radar (SAR) images and laboratory experiments on surface wave excitation by internal waves (Umeyama 2002). Including free surface conditions, a number of numerical models for long internal waves have been developed (Choi & Camassa 1996; Părău & Dias 2001; Lynett & Liu 2002*b*; Nguyen & Dias 2008; Liu & Wang 2012). However, considerably less attention has been paid to free surface dynamics.

As further suggested by Lamb (1932), studying the interaction between internal and surface waves entails consideration of higher-order interactions; these have also been explored experimentally (Joyce 1974; Lewis, Lake & Ko 1974) and theoretically (Ma 1982; Donato, Peregrine & Stocker 1999; Liu 2006; Selezov *et al.* 2010; Craig, Guyenne & Sulem 2011). The triad resonance interaction is also of interest to some researchers (Hill & Foda 1998; Alam 2012). Most of the aforementioned numerical models consist of two sets of equations generated by a two-layer fluid system with matching conditions at the boundary, and they require more computational time and resources than one equation set (Lynett & Liu 2004).

A depth-integrated approach for the shallow-water regime has been well established in the past few decades to represent the vertical structure of physical quantities as polynomials, and it successfully describes weakly dispersive waves. For the purpose of efficient but physically accurate modelling of surface waves over varying density, in the present study a new model based on depth integration is developed which includes both the effects on the surface waves from density variation as well as internal motion at the interface of two immiscible fluids of different densities. As these are general Boussinesq-type (small parameter perturbation) models, density-variation effects on the free surface are included as a correction term. In other words, direct inclusion of internal kinematics as weak components into the vertical flow structure allows a consistent representation of internal wave effects on surface wave physics. Throughout the derivation of the model equations, long-wave assumptions for both surface and internal waves are also made. Thus, the present model is designed to study the problem of weakly dispersive waves propagating over density-varying fluids.

This paper is organized as follows. In the following section, depth-integrated model equations for long surface waves over a variable-density fluid are derived mathematically, while their numerical solution uses an established numerical scheme and is provided in the supplementary materials available at http://dx.doi.org/10.1017/jfm.2014.144.Some limiting cases of the derived model are then investigated in § 3. Next, the numerical model is applied to surface wave propagation over either a horizontally or a vertically varying density field. An exercise to investigate the nonlinear properties of the designed model has also been performed for surface and internal wave interactions. The results are then compared with experimental and analytical data for the model validation. Final conclusions are presented in § 5.

## 2. Mathematical formulation

A mathematical model for weakly dispersive wave propagation over a varying-density fluid is derived in this section. A standard Boussinesq-type approach (e.g. Lynett & Liu 2002*a*; Kim, Lynett & Socolofsky 2009) is followed during the derivation to obtain a vertically independent equation set. Note that here we use the term 'Boussinesq' as related to weakly dispersive and nonlinear; we are not implying the same namesake commonly referenced in the oceanography field when including buoyancy effects.

https://doi.org/10.1017/jfm.2014.144 Published online by Cambridge University Press

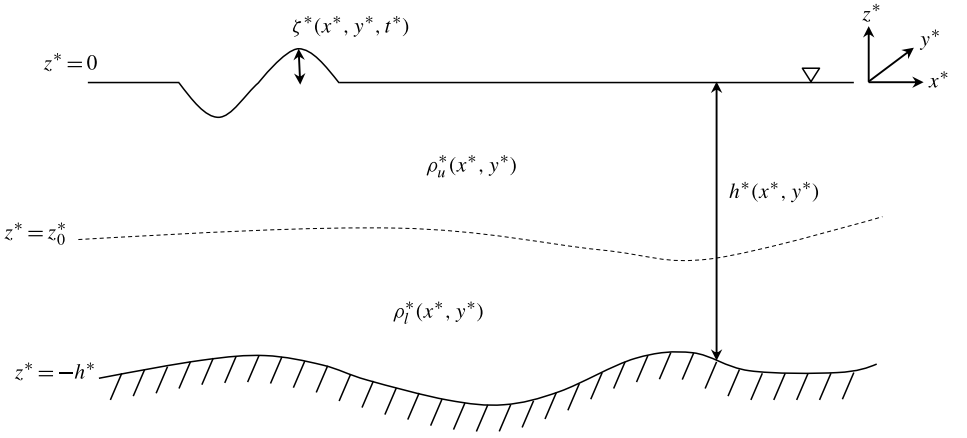



FIGURE 1. Sketch of long-wave propagation over two-layer fluids with horizontal density variation.

### 2.1. *Governing physics and boundary conditions*

To derive a mathematical governing system of equations, the basic physical parameters are defined as in figure 1. A two-layer fluid stably separated by a pycnocline of small, but finite, thickness is assumed to be incompressible and immiscible. Appropriate parametric scales are now introduced to normalize the governing equations as well as boundary conditions. As is typical for long-wave scaling, the wavelength $\ell_0$ and water depth $h_0$ are used for horizontal and vertical coordinates, respectively. Additionally, $\rho_b$ is a characteristic fluid density of the entire fluid system. Using this set of scaling parameters, we introduce the normalized variables

$$\left.\begin{aligned} (x, y) = \frac{(x', y')}{\ell_0}, \quad z = \frac{z'}{h_0}, \quad \zeta = \frac{\zeta'}{h_0}, \quad h = \frac{h'}{h_0}, \quad t = \frac{t'\sqrt{gh_0}}{\ell_0}, \\ (u, v) = \frac{(u', v')}{\sqrt{gh_0}}, \quad w = \frac{w'}{\mu\sqrt{gh_0}}, \quad p = \frac{p'}{\rho_b g h_0}, \quad \rho = \frac{\rho'}{\rho_b}, \\ \mu = \frac{h_0}{\ell_0}, \quad \nu_t^h = \frac{\nu_t^{h'}}{\alpha h_0\sqrt{gh_0}}, \quad \nu_t^v = \frac{\nu_t^{v'}}{\beta h_0\sqrt{gh_0}}, \end{aligned}\right\} \tag{2.1}$$

where a prime denotes a dimensional variable, and $(u, v)$ and $w$ represent instantaneous horizontal and vertical velocity, respectively. Here $\zeta$ is the free surface elevation, which is a function of $(x, y, t)$, $p$ is pressure, $g$ is the acceleration due to gravity and $\rho$ is density. Dimensionless parameters $\alpha$ and $\beta$ are used to scale the horizontal and vertical eddy viscosities $\nu_t^h$ and $\nu_t^v$ (Kim *et al.* 2009), and velocities are scaled following long-wave theory. Note that there is no wave amplitude scale, which would otherwise appear in the $\zeta$, pressure and velocity scalings; it is implicitly assumed that the wave amplitude is of the same order as the water depth.

To examine the effects of spatially variable density on free surface waves, it is necessary to parametrize the magnitude of the density change. To quantify the density variation we introduce the parameter

$$\gamma = \frac{\Delta\rho'}{\rho_b}. \tag{2.2}$$

The term $\Delta\rho'$ is simply the characteristic density variation in the physical system to be examined.

https://doi.org/10.1017/jfm.2014.144 Published online by Cambridge University Press

Following Kim *et al.* (2009), we obtain the dimensionless form of the spatially filtered continuity and Navier–Stokes equations for incompressible flow:

$$\nabla \cdot \boldsymbol{u} + w_z = 0, \tag{2.3}$$

$$\rho(\boldsymbol{u}_t + \boldsymbol{u} \cdot \nabla \boldsymbol{u} + w\boldsymbol{u}_z) + \nabla p = \alpha\mu \nabla \cdot (\rho \nu_t^h \nabla \boldsymbol{u}) + \frac{\beta}{\mu}(\rho \nu_t^v \boldsymbol{u}_z)_z, \tag{2.4}$$

$$\mu^2 \rho(w_t + \boldsymbol{u} \cdot \nabla w + w w_z) + p_z + \rho = \alpha\mu^3 \nabla \cdot (\rho \nu_t^h \nabla \omega) + \beta\mu(\rho \nu_t^v w_z)_z, \tag{2.5}$$

where $\nabla$ is the horizontal derivative operator, subscripts $z$ and $t$ function as vertical and time differentiations, respectively, and $\boldsymbol{u} = (u, v)$ is the horizontal velocity vector.

The conditions applied at the free surface and at the bottom boundary in figure 1 are expressed in dimensionless form, as well:

$$w = \zeta_t + \boldsymbol{u} \cdot \nabla \zeta \quad \text{at } z = \zeta, \tag{2.6}$$

$$w + \boldsymbol{u} \cdot \nabla h = 0 \quad \text{at } z = -h. \tag{2.7}$$

Equations (2.3)–(2.7) represent the primitive equation set needed to describe the fluid motion shown in figure 1.

### 2.2. *Boussinesq-type equations for nonlinear and dispersive waves over a variable-density fluid*

With a few dimensionless parameters introduced, $\mu^2$ is chosen to expand the physical variables. The assumption is made that the effects of density stratification and viscosity are weak and of an order similar to that of dispersion. That is,

$$O(\mu^2) = O(\mu\beta, \gamma) \ll 1. \tag{2.8}$$

This mathematical approximation is typical in long-wave studies (Lynett & Liu 2002*b*; Kim *et al.* 2009) and is used to drive a small parameter perturbation analysis.

To facilitate the final expression of our equations in a closed (non-integral) form, a functional restriction will be placed on the internal density field. Here a simple vertical density structure (figure 2) is assumed; however, this is sufficiently realistic to resemble a physical configuration found commonly in oceans and lakes (e.g. Kao, Pan & Renouard 1985). A two-layer density profile is thereby specified as

$$\rho(x, y, z) = \rho_0(x, y)\left\{1 - \gamma \tanh\left(\frac{z - z_0}{\delta}\right)\right\}, \tag{2.9}$$

where $\rho_0$ is an average density of the two-layer system, $z_0$ is the midpoint of the tanh inflection separating the upper and lower layers, and $\delta$ is the finite transition pycnocline thickness. Note that all terms in the above density profile expression are dimensionless; density has been scaled by $\rho_b$ and the three distance terms inside the tanh operator have been scaled by the depth, $h$. A discrete two-layer density configuration thus can be accommodated using the tanh function, eliminating any density discontinuity issues. In addition, the horizontal velocity of the background internal motion, $\boldsymbol{u}^i(z)$, is included to extend the derivation to include internal motion resulting from stratification.

With a specified density field and internal velocity field, a perturbation analysis followed by a depth integration is performed on (2.3)–(2.5). The derivation steps are somewhat tedious, make use of an established technique (e.g. Kim *et al.* 2009), and

https://doi.org/10.1017/jfm.2014.144 Published online by Cambridge University Press

are included with detail in the supplementary materials. The resulting depth-integrated mass and momentum equations are, respectively,

$$\zeta_t + \nabla \cdot \{(\zeta + h)\boldsymbol{u}_\alpha\} + \mu^2(\mathscr{N}_D + \mathscr{N}_B + \mathscr{N}_I) = O(\mu^4), \tag{2.10}$$

$$\begin{aligned}(\boldsymbol{u}_\alpha)_t + \boldsymbol{u}_\alpha \cdot \nabla \boldsymbol{u}_\alpha + \nabla\zeta + \frac{\nabla\rho_0}{\rho_0}\frac{(\zeta+h)}{2} + \gamma\mathscr{R}_P^v + \mu^2(\mathscr{R}_D + \mathscr{R}_B + \mathscr{R}_I + \mathscr{R}_P^h + \overline{\xi}) \\ - \alpha\mu\frac{1}{\rho_0}\nabla\cdot(\rho_0\nu_t^h\nabla\boldsymbol{u}_\alpha) + \beta\mu\nu_t^v\nabla S + \beta\mu\frac{1}{\rho_0}\frac{\tau_b}{\zeta+h} - \beta\mu\nu_t^v\{(\boldsymbol{u}^i)_z|_{z=\zeta} - (\boldsymbol{u}^i)_z|_{z=-h}\} \\ = O(\mu^4, \alpha\mu^3, \beta\mu^3),\end{aligned} \tag{2.11}$$

in which $\boldsymbol{u}_\alpha$ is the horizontal velocity vector evaluated at $z = z_\alpha = -0.531h$ (Nwogu 1993), $S = (\nabla \cdot \boldsymbol{u}_\alpha)$ and $\tau_b$ is bottom stress. In equations (2.10) and (2.11), each higher-order term implies weak effects from frequency dispersion ($\mathscr{N}_D$, $\mathscr{R}_D$), bottom stress ($\mathscr{N}_B$, $\mathscr{R}_B$), internal motion ($\mathscr{N}_I$, $\mathscr{R}_I$) and density variation ($\mathscr{R}_P^h$ and $\mathscr{R}_P^v$). Relevant definitions can be found in the supplementary materials. Removing terms related to density variation and internal motion yields a model identical to that in Kim *et al.* (2009).

## 3. Limiting cases of the derived model

### 3.1. *Linear inviscid equations*

Eliminating all nonlinear terms in $\zeta$ and $\boldsymbol{u}_\alpha$, assuming that $\zeta/h$ is very small, and converting to dimensional form yields the linear system

$$\begin{aligned}\zeta_t + \nabla\cdot(h\boldsymbol{u}_\alpha) - \nabla\cdot\left[\left(\frac{h^3}{6} - \frac{hz_\alpha^2}{2}\right)\nabla S - \left(\frac{h^2}{2} + hz_\alpha\right)\nabla T\right] \\ + \nabla\cdot(h\overline{\boldsymbol{u}^i}) = 0,\end{aligned} \tag{3.1}$$

$$\begin{aligned}(\boldsymbol{u}_\alpha)_t + g\nabla\zeta + \tfrac{1}{2}z_\alpha^2\nabla S_t + z_\alpha\nabla T_t \\ + \overline{\boldsymbol{u}_t^i} + \nabla(\boldsymbol{u}_\alpha\cdot\overline{\boldsymbol{u}^i}) \\ + \frac{\nabla\rho_0}{\rho_0}\left[\frac{gh}{2} + \left(\frac{h^2}{6}S_t - \frac{h}{2}T_t\right)\right] + (\mathscr{R}_P^v)_{linear} = 0,\end{aligned} \tag{3.2}$$

where $g$ is the acceleration due to the gravity and $(\mathscr{R}_P^v)_{linear}$ is constructed in the same manner as $\mathscr{R}_P^v$, with the differences being the nonlinear $\boldsymbol{u}_\alpha \cdot \nabla\boldsymbol{u}_\alpha$ term removed and all $\zeta$ set to zero. Both of the above equations are presented such that the standard, free surface-only wave terms are shown in the first line, and the terms driven by the internal flow and stratification are given in the subsequent lines. In the second line of the linear momentum equation (3.2) above are the forcing terms associated with the depth-averaged internal flow, while in the third line are the two terms attributed to horizontal and vertical density gradients, respectively.

### 3.2. *First-order nonlinear inviscid equations*

Here, we include only first-order nonlinear terms; $\zeta/h$ is no longer negligible. The dimensional system becomes

$$\begin{aligned}\zeta_t + \nabla\cdot(H\boldsymbol{u}_\alpha) - \nabla\cdot\left[\left(\frac{h^3}{6} - \frac{Hz_\alpha^2}{2}\right)\nabla S - \left(\frac{h^2}{2} + Hz_\alpha\right)\nabla T\right] \\ + \nabla\cdot(H\overline{\boldsymbol{u}^i}) = 0,\end{aligned} \tag{3.3}$$

https://doi.org/10.1017/jfm.2014.144 Published online by Cambridge University Press

$$(\boldsymbol{u}_\alpha)_t + \boldsymbol{u}_\alpha \cdot \nabla \boldsymbol{u}_\alpha + g\nabla\zeta + \tfrac{1}{2}z_\alpha^2 \nabla S_t + z_\alpha \nabla T_t$$
$$- \nabla(\zeta T_t) + T\nabla T + \tfrac{1}{2}\nabla(z_\alpha^2 \boldsymbol{u}_\alpha \cdot \nabla S) + \nabla(z_\alpha \boldsymbol{u}_\alpha \cdot \nabla T)$$
$$+ \overline{\boldsymbol{u}^i_t} + \nabla(\boldsymbol{u}_\alpha \cdot \overline{\boldsymbol{u}^i}) + \mathscr{R}_P^v$$
$$+ \frac{\nabla\rho_0}{\rho_0} \times \left\{ \frac{gH}{2} + \left[ \frac{-\zeta h}{6} S_t + \frac{h^2}{6}(S_t + \boldsymbol{u}_\alpha \cdot \nabla S - S^2) \right.\right.$$
$$\left.\left. - \frac{1}{2}\zeta T_t - \frac{h}{2}(T_t + \boldsymbol{u}_\alpha \cdot \nabla T - ST) \right] \right\} = 0, \tag{3.4}$$

where $H = h + \zeta$. Again, the standard Boussinesq-type terms are given first in the above equations. This nonlinear system will be analysed later in the paper to determine its analytical behaviour. It is noted here that, in the absence of any vertical or horizontal density gradient, all 'new' terms disappear, with the exception of the $\overline{\boldsymbol{u}^i}$ term in both the continuity and momentum equations. Although these terms have been discussed in this paper in the framework of internal motion, the effects of any type of imposed external flow could be accommodated through $\overline{\boldsymbol{u}^i}$.

## 4. Model validation

In this section, the model is applied to various types of problems in which the fluid density field is configured to vary either horizontally or vertically. Calculated results from these simulations are then compared to experimental data or analytical solutions for verification. Complete details of the numerical scheme used in the following examples can be found in the supplementary materials; in brief, the time integration and spatial discretization are fourth-order accurate, and make use of a finite-volume method. Note that for the remainder of the paper, as simplified analytical and laboratory cases are examined, all terms related to viscosity (with coefficients $\alpha$ or $\beta$) are neglected.

### 4.1. *Horizontally varying fluid density: pneumatic breakwater*

In this section, free surface wave propagation in a fluid with a horizontal density gradient is considered. The fluid is assumed to be well mixed vertically such that stratification effects ($\mathscr{R}_I$ and $\mathscr{R}_P^v$) can be ignored. Although this physical set-up is a reasonable representation of common coastal situations (e.g. wind waves near a river mouth or inside an estuary), published experimental data in this configuration are very limited. The reason for this lack of available data is probably due to the complexity of the experimental set-up; a horizontal density gradient is not stable, and continuous forcing is required to maintain it. With this in mind, the model derived here will be compared with the available data such that the behaviour of the model might be assessed. Data from a two-phase flow (air/water), pneumatic breakwater experiment are chosen. The bubbly area around the pneumatic breakwater is regarded as the low-density fluid while the surrounding clear water maintains a constant density.

Most studies of pneumatic breakwaters focus on the surface currents generated by bottom-generated bubbly flows, which are believed to be the main drivers of wave attenuation (Taylor 1955; Lo 1991). Nonetheless, a sudden density drop in the bubbly zone is responsible for some wave energy blockage, in that less momentum can be transported through the lower-density bubbly fluid. Herein, the present model is applied to a pneumatic breakwater simulation, in which horizontal density gradient effects in wave attenuation are evaluated.

https://doi.org/10.1017/jfm.2014.144 Published online by Cambridge University Press

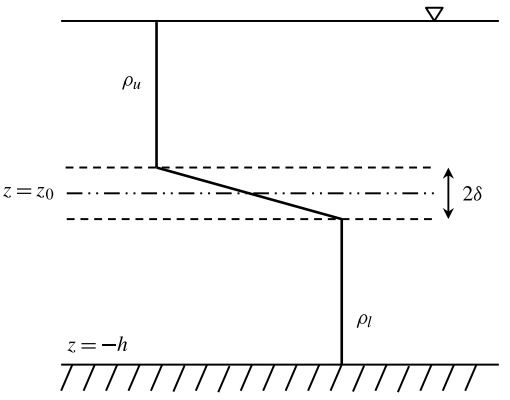



FIGURE 2. Idealized density structure of a two-layer fluid system.

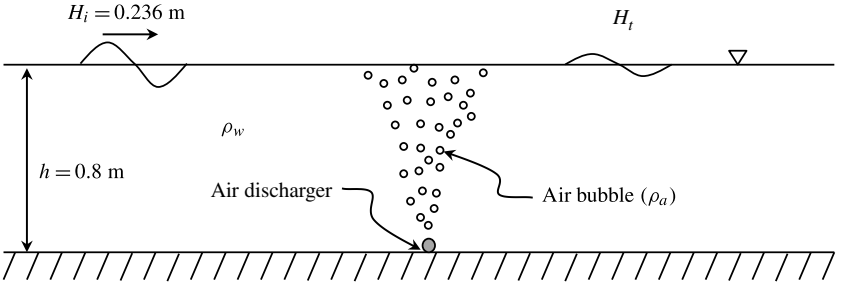



FIGURE 3. Experimental set-up of the pneumatic breakwater (Zhang *et al.* 2010).

| | |
|---|---|
| Water depth | 0.8 m |
| Wave height | 0.236 m |
| Wave period | 1.29, 1.55 s |
| Air amount | 10, 20, 30, 40 $m^3\ h^{-1}$ |

TABLE 1. Experimental conditions for the pneumatic breakwater (Zhang *et al.* 2010).

There are a few laboratory studies on pneumatic breakwaters (e.g. Straub, Bowers & Tarapore 1959; Bulson 1963; Zhang *et al.* 2010). Among these, Zhang *et al.* (2010) carried out a laboratory test on the performance of pneumatic breakwaters at a 1 : 15 model scale. Using relatively long incident waves, they measured the wave height behind the pneumatic breakwater to quantify wave transmission through the bubble system. Figure 3 shows the experimental set-up of the pneumatic breakwater. The wave tank has dimensions of 2 m in width, 1.8 m in depth and 69 m in length, and the air discharge pipe is installed along the bottom. Through orifices of 0.8 mm diameter, spaced 0.01 m along the pipe, air is discharged into the water to create a bubble curtain. To examine the breakwater performance as a function of different hydraulic conditions, two different wave periods and four different air fluxes are tested. Table 1 summarizes the experimental conditions on the laboratory scale.

For the numerical simulation, a computational domain based on the wave tank dimensions is constructed using $\Delta x = 0.025$ m. A flexible time step, $\Delta t$, is adopted

https://doi.org/10.1017/jfm.2014.144 Published online by Cambridge University Press

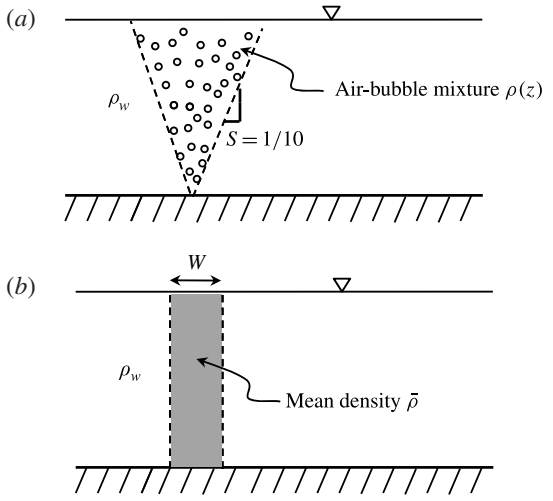



FIGURE 4. Simplified density field of bubbly fluids for (*a*) depth-varying $\rho(z)$ and (*b*) depth-constant $\overline{\rho}$.

according to the Courant–Friedrichs–Lewy stability condition. During the simulation, the transmitted wave height is measured behind the low-density region. One remaining issue in creating the numerical configuration is to conceptualize the bubbly field into an 'equivalent' fluid zone of low density. To this end, some simplifying assumptions are made. For shallow flows, the lateral distribution of bubble concentration at any depth is given by a top-hat profile. Moreover, as seen in figure 4(*a*), bubbles are assumed to be scattered, forming a linear slope (=1/10) under the wavy condition, as indicated in Zhang *et al.* (2010). The slip velocity ($u_s$) of the rising bubble is given empirically by (Clift, Grace & Weber 1978)

$$u_s = \begin{cases} 4474\ \text{m s}^{-1} \times r_b^{1.357} & \text{if } 0 \leqslant r_b \leqslant 0.7\ \text{mm}, \\ 0.23\ \text{m s}^{-1} & \text{if } 0.7 < r_b \leqslant 5.1\ \text{mm}, \\ 4.202\ \text{m s}^{-1} \times r_b^{0.547} & \text{if } r_b > 5.1\ \text{mm}, \end{cases} \tag{4.1}$$

where $r_b$ is the bubble radius, which is approximately the same as the orifice radius (Ma, Shi & Kirby 2011). The fluid velocity ($u_w$) is determined by (Milgram 1983)

$$u_w = 1.5 u_s. \tag{4.2}$$

The total rising velocity of bubbles is then $(u_s + u_w)$.

Guided by these assumptions, we can calculate the density of the bubbly zone as

$$\rho(z) = \left\{ 1 - \frac{q_a}{2\mathscr{S}(h+z)(u_s+u_w)} \right\} \rho_w + \frac{q_a}{2\mathscr{S}(h+z)(u_s+u_w)} \rho_a, \tag{4.3}$$

where $\rho_a$ and $\rho_w$ represent the densities of air (1.269 kg m$^{-3}$) and water (1000 kg m$^{-3}$), respectively, $\mathscr{S}$ denotes the side slope of the bubbly zone, and $q_a$ represents the injected air volume per unit width. For depth-integrated model use, $\rho(z)$ is depth-averaged, as depicted in figure 4(*b*). The calculated quantities for density fields are listed in table 2.

The computed results for the transmission coefficient $K_t$ (transmitted wave height divided by incident wave height) are plotted in figures 5 and 6 with the measurements. As expected, the effects of the density transition can be found in both results,

https://doi.org/10.1017/jfm.2014.144 Published online by Cambridge University Press

| Air amount, $q_l$ ($m^3\ h^{-1}\ m^{-1}$) | Slip velocity, $u_s$ ($m\ s^{-1}$) | Fluid velocity, $u_w$ ($m\ s^{-1}$) | $\overline{\rho}$ | Width, $W$ (m) |
|---|---|---|---|---|
| 5 | 0.11 | 0.67 | 938.52 | 0.08 |
| 10 | 0.11 | 0.67 | 880.77 | 0.08 |
| 15 | 0.11 | 0.67 | 826.20 | 0.08 |
| 20 | 0.11 | 0.67 | 774.89 | 0.08 |

TABLE 2. Parameters for simplified density fields of the bubbly area.

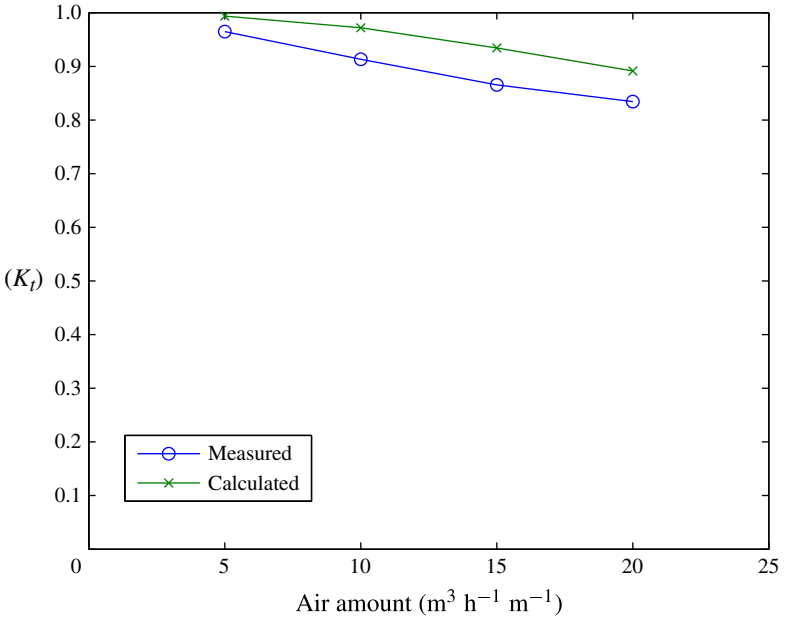



FIGURE 5. (Colour online) Comparison of transmission coefficient ($K_t$) between measurement and calculation; $T = 1.55$ s.

indicating that greater air volume discharge yields less transmission through the pneumatic breakwater. Comparison between calculation and measurement shows good agreement, although the numerical simulations have a clear overprediction bias. The likely reason for this discrepancy is the numerical neglect of the bubble-induced currents. However, the model provides the proper parametric trends and dependences, and the accuracy is reasonable.

### 4.2. *Waves excited by internal motion: linear surface waves*

In this section, we consider a two-layer internal flow in which an internal wave travels along the interface. Because we are concerned with vertical stratification only, terms associated with horizontal density variation ($\mathscr{R}_P^h$) are neglected. It is well known that the presence of interfacial motion in a two-layer fluid excites free surface motion (Lamb 1932; Phillips 1977). Lamb (1932) obtained an exact solution for the surface disturbance resulting from an internal wave using linear potential theory. Such disturbances at the free surface propagate along with internal waves, whose dispersive properties are locked to the internal motion.

https://doi.org/10.1017/jfm.2014.144 Published online by Cambridge University Press

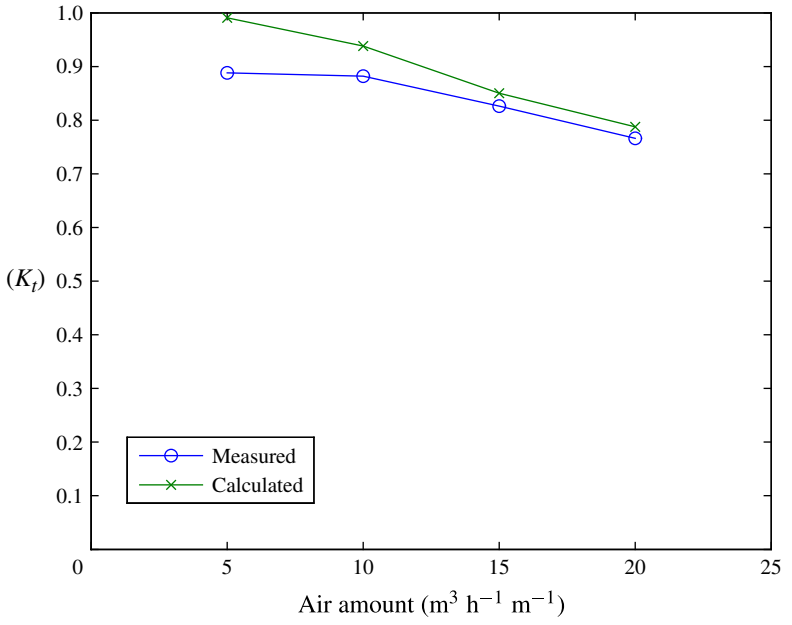



FIGURE 6. (Colour online) Comparison of transmission coefficient ($K_t$) between measurement and calculation; $T = 1.29$ s.

Within the presented derivation, the profile $u^i(z)$ has up to this point been considered arbitrary. To account for internal wave effects on the free surface modes, a reasonable description of the internal wave velocity $u^i(z)$ is needed here. First, the simplified two-layer system as shown in figure 7 is presented. The density and the undisturbed thickness of the upper layer are $\rho_u$ and $h_u$, while those of the lower layer are $\rho_l$ and $h_l$. The disturbances propagating along the surface ($\eta^s$) and interface ($\eta^i$) are defined simply as

$$\eta^s = a^s \cos \vartheta^i, \tag{4.4}$$

$$\eta^i = a^i \cos \vartheta^i, \tag{4.5}$$

where $a^s$ and $a^i$ represent wave amplitudes at the surface and interface, respectively, and $\vartheta^i$ $(= k^i x - \sigma^i t + \epsilon)$ is the phase function with arbitrary shift $\epsilon$. Note that $k^i$ and $\sigma^i$ are assumed to follow the internal wave dispersion relation (Lamb 1932)

$$\left\{ \frac{\rho_u}{\rho_l} \tanh(k^i h_u) \tanh(k^i h_l) + 1 \right\} (\sigma^i)^4 - g k^i \left\{ \tanh(k^i h_u) + \tanh(k^i h_l) \right\} (\sigma^i)^2 + \tanh(k^i h_u) \tanh(k^i h_l) \left( 1 - \frac{\rho_u}{\rho_l} \right) g^2 (k^i)^2 = 0. \tag{4.6}$$

Following Liu (2006), who developed an analytic solution based on potential theory, we can express the linear solution of $u^i$ as

$$u^i(z) = \begin{cases} [A \cosh \{k^i(z + h_l)\} + B \sinh \{k^i(z + h_l)\}] \cos \vartheta^i & (\eta^i \leqslant z \leqslant \eta^s), \\ C \cosh \{k^i(z + h_u + h_l)\} \cos \vartheta^i & (-h_l \leqslant z \leqslant \eta^i), \end{cases} \tag{4.7}$$

https://doi.org/10.1017/jfm.2014.144 Published online by Cambridge University Press

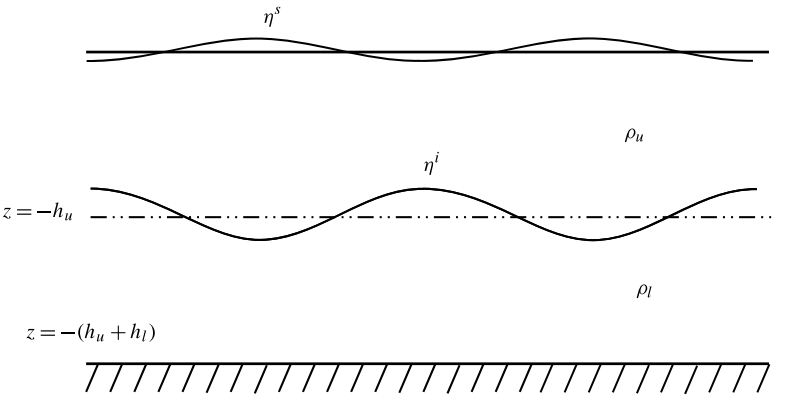



FIGURE 7. Simplified two-layer system with an interfacial wave. The assumption underlying the plot is that an internal-mode interfacial wave ($\eta^i$) generates an internal-mode surface wave ($\eta^s$). For the definition of internal mode, see Părău & Dias (2001).

where $A$, $B$ and $C$ are

$$A = \frac{a^i}{\sigma^i}\left[g\left(1-\frac{\rho_l}{\rho_u}\right)+\frac{\rho_l(\sigma^i)^2}{\rho_u k^i \tanh(k^i h_l)}\right], \tag{4.8}$$

$$B = \frac{a^i\sigma^i}{k^i}, \tag{4.9}$$

$$C = \frac{a^i\sigma^i}{k^i \sinh(k^i h_l)}. \tag{4.10}$$

The depth-averaged internal velocity, $\overline{u^i}$, is needed by the model; it can be calculated as

$$\begin{aligned}\overline{u^i} &= \frac{1}{h_u+h_l}\int_{-(h_u+h_l)}^{\eta^s} u^i(z)\,\mathrm{d}z \\ &= \frac{\sigma^i}{k^i(h_u+h_l)}\left\{\frac{\sigma^i}{(\sigma^i)^2\cosh(k^i h_u)-gk^i\sinh(k^i h_u)}\right\}a^i\cos\vartheta^i\end{aligned} \tag{4.11}$$

from linear theory. By using the relationship between $a^i$ and $a^s$ (Lamb 1932; Liu 2006)

$$a^s = \frac{\sigma^i}{(\sigma^i)^2\cosh(k^i h_u)-gk^i\sinh(k^i h_u)}a^i, \tag{4.12}$$

equation (4.11) can be further simplified to

$$\overline{u^i} = \frac{\sigma^i}{k^i(h_u+h_l)}\eta^s. \tag{4.13}$$

As only linear internal waves are examined, any nonlinear correction for large-amplitude waves is neglected. With the above solution, however, it can be deduced that two-layer internal waves produce a mean instantaneous flux that excites linear surface motion. The above expression for the depth-averaged internal velocity, when

https://doi.org/10.1017/jfm.2014.144 Published online by Cambridge University Press

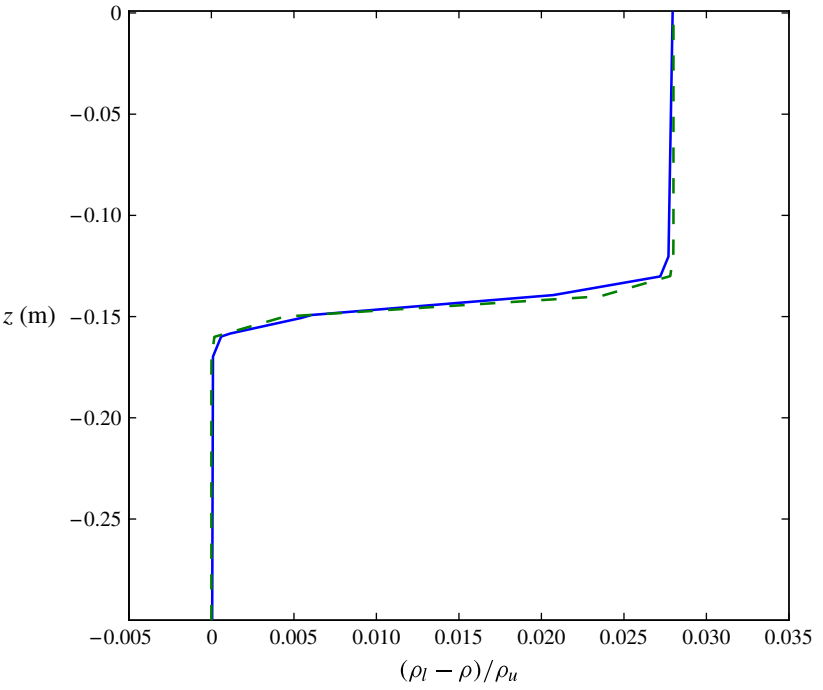



FIGURE 8. (Colour online) Measured (solid) and approximated (dashed) density profile from Umeyama (2002).

used in the derived model, will produce locked surface modes that should reproduce the linear dispersive solution above exactly. If one assumes that the water depth is constant, that the density has no gradient in the horizontal plane, and that there exists only the internal-mode free surface wave, whose dispersion property is locked to the internal waves, equation (4.13) can be exactly obtained. Also note that, for other types of internal wave structures (e.g. solitary waves), $\overline{u^i}$ can be straightforwardly obtained and applied to the model, but this will not be presented here.

We next examine surface movement excitation resulting from internal motion using experimental and numerical data. For laboratory data, the data of Umeyama (2002) are used here. He used a 3 m long, 0.15 m wide and 0.22 m deep wave tank equipped with an oil-pressure-type wave maker on one end and a wave absorber on the other to generate internal waves. The density profile measured in the experiment is re-created and shown in figure 8, with the approximated value from (2.9) for comparison. Since the pycnocline thickness is found to be extremely small ($\delta = \delta'/h' = 0.006$ m/0.30 m $= 0.02$), the $\mathscr{R}_P^v$ term, which is $O(\mu^2\delta)$, can be neglected. Table 3 summarizes the test conditions of the experiment. It should be noted here that internal waves propagate as the internal-mode waves of (4.6). There is no external-mode wave either at the surface or at the interface. Note that, in referring to internal and external modes, we follow Părău & Dias's (2001) guidance.

The physical layout of the experiment is mapped to the computational domain for numerical implementation; $\Delta x = 0.02$ m and $\Delta t = 0.002$ s have been chosen. Simulated results of the free surface elevation induced by internal waves are presented in figures 9 and 10, and both experimental data and analytical solutions (4.12) are included for comparison. The expected agreement between numerical and analytical

https://doi.org/10.1017/jfm.2014.144 Published online by Cambridge University Press

| | Case I | Case II |
|---|---|---|
| Wave amplitude, $a^i$ (m) | 0.005 | 0.005 |
| Wave period, $T^i$ (s) | 5.4 | 6.4 |
| Lower layer thickness, $h_l$ (m) | 0.15 | 0.15 |
| Upper layer thickness, $h_u$ (m) | 0.15 | 0.15 |
| Pycnocline thickness, $\delta$ (m) | 0.006 | 0.006 |
| Lower layer density, $\rho_l$ (kg m$^{-3}$) | 1050 | 1050 |
| Upper layer density, $\rho_u$ (kg m$^{-3}$) | 1000 | 1000 |

TABLE 3. Experimental conditions for internal waves in a two-layer fluid (Umeyama 2002).

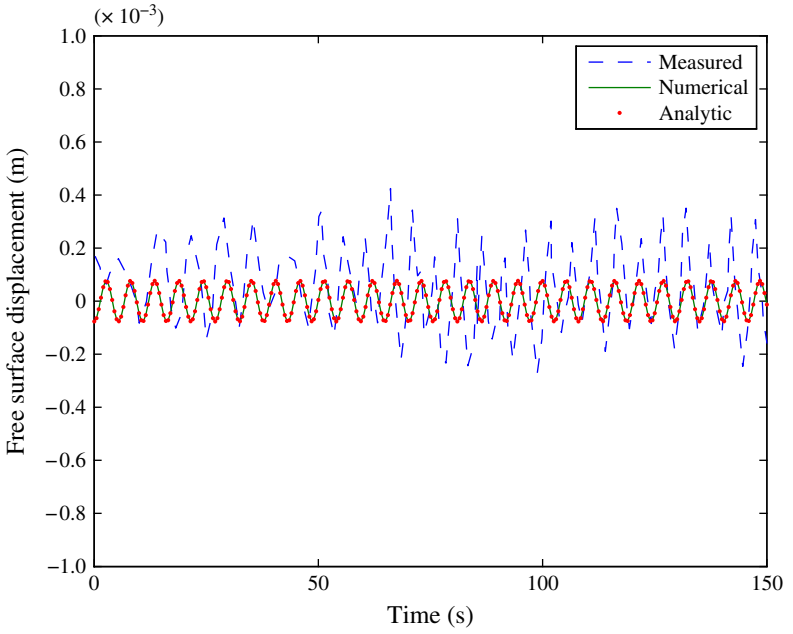



FIGURE 9. (Colour online) Measured (dashed), numerical (solid) and analytical (dotted) surface elevation for Case I.

results is found. Some disagreement with measurement is seen in both the magnitude and the phase of the free surface waves. Given the small scale and measurement complexity in these laboratory tests, the calculation gives reasonable results.

### 4.3. *Waves excited by internal motion: nonlinear surface waves*

As explored in the previous section, surface waves are generated by internal waves according to linear solutions. These waves are locked to the phase of the internal waves and are therefore linearly governed by the internal wave dispersion relation. In a more general situation where free gravity waves, such as wind waves or tsunamis, propagate on the surface, there may exist some nonlinear coupling between these two modes. Thus, in this section, the nonlinear interaction between internal- and external-mode surface waves is investigated. This analysis will rely on quantifying the analytical behaviour of the first-order nonlinear system, as given in § 3.2.

https://doi.org/10.1017/jfm.2014.144 Published online by Cambridge University Press

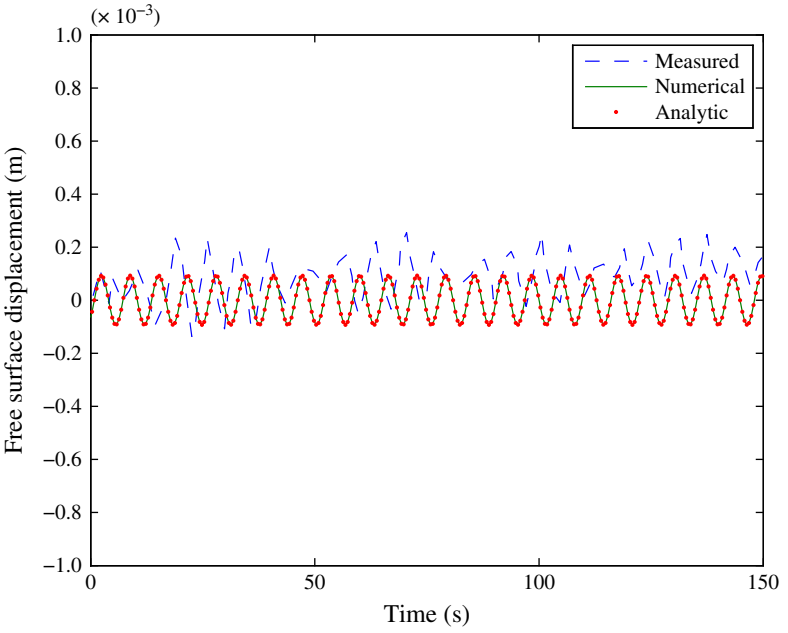



FIGURE 10. (Colour online) Measured (dashed), numerical (solid) and analytical (dotted) surface elevation for Case II.

Similar nonlinear analyses performed previously for Boussinesq-type equations can be found in, for example, Kennedy *et al.* (2001) and Lynett & Liu (2004). Stokes theory is a well-defined and easily used method that can be appropriately adopted here. As follows from Kennedy *et al.* (2001), the first-order nonlinear equation model in one horizontal dimension, with constant depth, and weak horizontal and vertical density gradients, is given as

$$\begin{aligned}
&(\zeta^{[2]})_t + h(u_\alpha^{[2]})_x + h^3\left\{\frac{1}{2}\left(\frac{z_\alpha}{h}\right)^2 + \frac{z_\alpha}{h} + \frac{1}{3}\right\}(u_\alpha^{[2]})_{xxx} \\
&\quad = -[\zeta^{[1]}u_\alpha^{[1]}]_x - h^2\left\{\frac{1}{2}\left(\frac{z_\alpha}{h}\right)^2 + \frac{z_\alpha}{h}\right\}[\zeta^{[1]}\left(u_\alpha^{[1]}\right)_{xx}]_x - [\zeta^{[1]}\overline{u^i}]_x, \qquad (4.14)\\
&(u_\alpha^{[2]})_t + g(\zeta^{[2]})_x + h^2\left\{\frac{1}{2}\left(\frac{z_\alpha}{h}\right)^2 + \frac{z_\alpha}{h}\right\}(u_\alpha^{[2]})_{xxt} \\
&\quad = -u_\alpha^{[1]}(u_\alpha^{[1]})_x + h[\zeta^{[1]}(u_\alpha^{[1]})_{xt}]_x - h^2\left\{\frac{1}{2}\left(\frac{z_\alpha}{h}\right)^2 + \frac{z_\alpha}{h}\right\}[u_\alpha^{[1]}(u_\alpha^{[1]})_{xx}]_x \\
&\qquad - \frac{1}{2}h^2[(u_\alpha^{[1]})_x{}^2]_x - (u_\alpha^{[1]}\,\overline{u^i})_x, \qquad (4.15)
\end{aligned}$$

where the superscripts [1] and [2] represent first- and second-order solutions in the Stokes system, respectively. Suppose that there are internal- and external-mode surface waves expressed as

$$\zeta^{[1]} = \zeta^e + \zeta^i = a^e\cos\vartheta^e + a^i\cos\vartheta^i, \qquad (4.16)$$

$$u_\alpha^{[1]} = b^e\cos\vartheta^e, \qquad (4.17)$$

$$\overline{u^i} = b^i\cos\vartheta^i, \qquad (4.18)$$

https://doi.org/10.1017/jfm.2014.144 Published online by Cambridge University Press

where superscripts $i$ and $e$ imply internal- and external-mode components, respectively. Again, the internal-mode surface wave has been generated by internal interfacial waves, whereas the external-mode surface wave is assumed to be a free gravity wave on the air–fluid surface. The amplitude of the free surface displacement and velocity are symbolized by $a$ and $b$, respectively.

Second-order solutions are then assumed as

$$\zeta^{[2]} = a^{ee}\cos(2\vartheta^e) + a^{ii}\cos(2\vartheta^i) + a^{+}\cos(\vartheta^e + \vartheta^i) + a^{-}\cos(\vartheta^e - \vartheta^i), \quad (4.19)$$

$$u_\alpha^{[2]} = b^{ee}\cos(2\vartheta^e) + b^{ii}\cos(2\vartheta^i) + b^{+}\cos(\vartheta^e + \vartheta^i) + b^{-}\cos(\vartheta^e - \vartheta^i), \quad (4.20)$$

where superscripts $ii$ and $ee$ are for self-interactions, whereas $+$ and $-$ are for the super- and subharmonic components, respectively. The phase function is $\vartheta^{(i,e)} = k^{(i,e)}x - \sigma^{(i,e)}t + \epsilon^{(i,e)}$. By substituting the first- and second-order solutions into (4.14) and (4.15), and collecting super- and subharmonic terms, $a^{\pm}$ can be obtained as

$$a^{\pm} = \frac{M_{22}^{\pm}L_1^{\pm} - M_{12}^{\pm}L_2^{\pm}}{M_{11}^{\pm}M_{22}^{\pm} - M_{12}^{\pm}M_{21}^{\pm}}, \quad (4.21)$$

where

$$M_{11}^{\pm} = \sigma^e \pm \sigma^i, \quad (4.22)$$

$$M_{12}^{\pm} = -(k^e \pm k^i)h\left[1 - \left\{\frac{1}{2}\left(\frac{z_\alpha}{h}\right)^2 + \frac{z_\alpha}{h} + \frac{1}{3}\right\}\right](k^e \pm k^i)^2h^2, \quad (4.23)$$

$$M_{21}^{\pm} = -g(k^e \pm k^i), \quad (4.24)$$

$$M_{22}^{\pm} = (\sigma^e \pm \sigma^i)\left[1 - \left\{\frac{1}{2}\left(\frac{z_\alpha}{h}\right)^2 + \frac{z_\alpha}{h}\right\}(k^e \pm k^i)^2h^2\right], \quad (4.25)$$

$$L_1^{\pm} = \frac{1}{2}(k^e \pm k^i)\left[a^ib^e + a^eb^i - \left\{\frac{1}{2}\left(\frac{z_\alpha}{h}\right)^2 + \frac{z_\alpha}{h}\right\}a^ib^e\,(k^eh)^2\right], \quad (4.26)$$

$$L_2^{\pm} = \frac{1}{2}(k^e \pm k^i)[b^ib^e - a^ib^ek^eh\sigma^e]. \quad (4.27)$$

This solution may be compared with an exact potential solution of Liu (2006), who derived second-order analytical expressions for internal and surface waves in a two-layer density-stratified fluid. By manipulating Liu's solution, the amplitude of super- and subharmonic waves, $a_{exact}^{\pm}$, can be expressed straightforwardly.

Figure 11 presents a comparison of super- and subharmonic wave amplitudes between the presented model and the full potential solutions when $h_u = 0.5$, $h_l = 0.5$ and $\rho_u/\rho_l = 0.9$. The contours show the model accuracy relative to potential theory; values near 1.0 are desired. As expected with the derived, long-wave-based model, accurate results are seen at small wavenumbers and errors grow as wavenumber increases. Both superharmonic and subharmonic wave amplitudes tend to be underpredicted as wave dispersion increases. From this analysis, we conclude that nonlinear interaction between internal- and external-mode surface waves can be predicted reasonably within the range of $k^eh < 0.3$ and $k^ih < 0.7$.

## 5. Summary

By allowing horizontal and vertical variation of fluid density, a depth-integrated model for long gravity waves over a variable-density fluid has been developed in

https://doi.org/10.1017/jfm.2014.144 Published online by Cambridge University Press

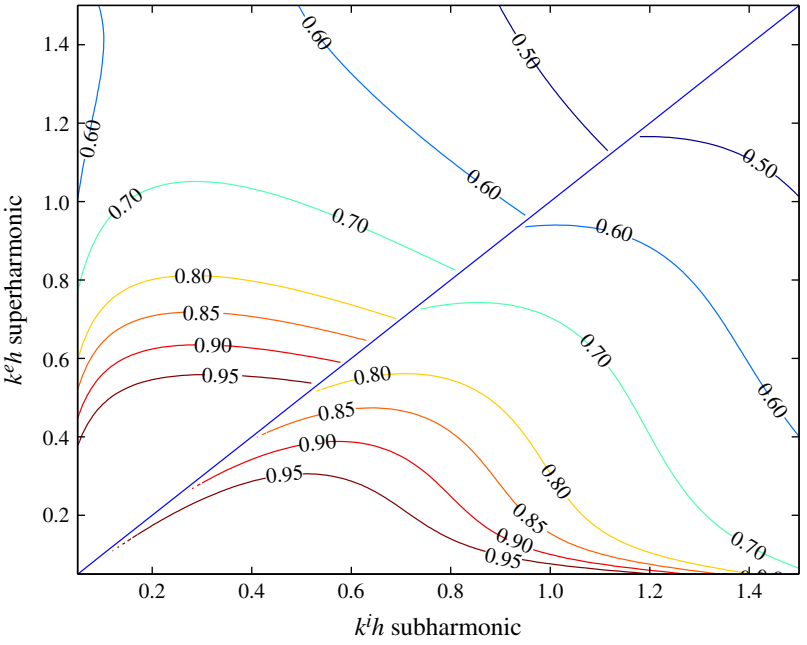



FIGURE 11. (Colour online) Second-order superharmonic and subharmonic amplitude relative to the exact solution ($a^{\pm}/a^{\pm}_{exact}$).

the present study.To include density variation effects, correction terms to represent horizontal and vertical density change are added to the typical Boussinesq-type model of uniform density. In particular, a two-layer fluid system is chosen to represent the vertical density variations, where interfacial wave effects on the free surface are additionally considered through direct inclusion of the velocity component of the interfacial wave. During the derivation of the equation set, the internal wave structure is kept in a generic form within the long-internal-wave approximation for general use. To numerically solve the derived equations, a finite-volume scheme coupled with an approximate Riemann solver is adopted for leading-order terms while cell-centred finite-volume methods are used for others.

The numerical model is applied to various types of problems in which the density field is configured to vary either horizontally or vertically. For horizontal variation of fluid density, a pneumatic breakwater system is simulated to assess density drop effects, and fair agreement is seen between computed and measured data, indicating that the current effect from the bubbly flux is responsible for wave attenuation to some degree. The interfacial wave of a two-layer fluid system, as a case of vertical density variation, is tested to investigate how the internal motion affects the free surface. As Lamb (1932) analysed, the surface disturbance caused by the internal wave is observed in the numerical results, which is in complete agreement with the analytical solution, and thus provides insight into how the internal motion within a two-layer fluid system affects surface motion. Lastly, the nonlinear interaction between external- and internal-mode surface waves is studied numerically and analytically, yielding a reasonable range of wavenumbers for practical application.

https://doi.org/10.1017/jfm.2014.144 Published online by Cambridge University Press

## Supplementary materials

Supplementary materials are available at http://dx.doi.org/10.1017/jfm.2014.144.

## REFERENCES


ALAM, M. R. 2012 A new triad resonance between co-propagating surface and interfacial waves. *J. Fluid Mech.* **691**, 267–278.

ARMI, L. & FARMER, D. 1986 Maximal two-layer exchange through a contraction with barotropic net flow. *J. Fluid Mech.* **164**, 27–51.

BULSON, P. S. 1963 Large scale bubble breakwater experiments. *Dock & Harbour Authority* **44** (516), 191–197.

CHOI, W. & CAMASSA, R. 1996 Weakly nonlinear internal waves in a two-fluid system. *J. Fluid Mech.* **313**, 83–103.

CHOI, W. & CAMASSA, R. 1999 Fully nonlinear internal waves in a two-fluid system. *J. Fluid Mech.* **384**, 27–58.

CLIFT, R., GRACE, J. & WEBER, M. 1978 *Bubbles, Drops and Particles*. Academic Press.

CRAIG, W., GUYENNE, P. & SULEM, C. 2011 Coupling between internal and surface waves. *Nat. Hazards* **57**, 617–642.

DEAN, R. G. & DALRYMPLE, R. A. 1984 *Water Wave Mechanics for Engineers and Scientists*. Prentice-Hall.

DEBSARMA, S., DAS, K. P. & KIRBY, J. T. 2010 Fully nonlinear higher-order model equations for long internal waves in a two-fluid system. *J. Fluid Mech.* **654**, 281–303.

DONATO, A. N., PEREGRINE, D. H. & STOCKER, J. R. 1999 The focusing of surface waves by internal waves. *J. Fluid Mech.* **384**, 27–58.

ELACHI, C. & APEL, J. R. 1976 Internal wave observations made with an airborne synthetic aperture imaging radar. *Geophys. Res. Lett.* **3** (11), 647–650.

ELDER, J. W. 1959 The dispersion of marked fluid in turbulent shear flow. *J. Fluid Mech.* **5**, 544–560.

EVANS, W. A. B. & FORD, M. J. 1996 An integral equation approach to internal (2-layer) solitary waves. *Phys. Fluids* **8**, 2032–2047.

FARMER, D. & ARMI, L. 1999 The generation and trapping of solitary waves over topography. *Science* **283**, 188–190.

GARGETT, A. E. & HUGHES, B. A. 1972 On the interaction of surface and internal waves. *J. Fluid Mech.* **52**, 179–191.

HELFRICH, K. & MELVILLE, W. 2006 Long nonlinear internal waves. *Annu. Rev. Fluid Mech.* **38**, 395–425.

HILL, D. F. & FODA, M. A. 1998 Subharmonic resonance of oblique interfacial waves by a progressive surface waves. *Proc. R. Soc. Lond.* A **454**, 1129–1144.

HWUNG, H.-H., YANG, R.-Y. & SHUGAN, I. V. 2009 Exposure of internal waves on the sea surface. *J. Fluid Mech.* **626**, 1–20.

JOYCE, T. M. 1974 Nonlinear interactions among standing surface and internal gravity waves. *J. Fluid Mech.* **63**, 801–825.

KANARSK, Y. & MADERICH, V. 2003 A non-hydrostatic numerical model for calculation free-surface stratified flows. *Ocean Dyn.* **53**, 176–185.

KAO, T., PAN, F.-S. & RENOUARD, D. 1985 Internal solitons on the pycnocline: generation, propagation, and shoaling and breaking over a slope. *J. Fluid Mech.* **159**, 19–53.

KENNEDY, A. B., KIRBY, J. T., CHEN, Q. & DALRYMPLE, R. A. 2001 Boussinesq-type equations with improved nonlinear performance. *Wave Motion* **33**, 225–243.

KIM, D.-H., LYNETT, P. & SOCOLOFSKY, S. 2009 A depth-integrated model for weakly dispersive, turbulent, and rotational fluid flows. *Ocean Model.* **27** (3–4), 198–214.

KOOP, C. G. & BUTLER, G. 1981 An investigation of internal solitary waves in a two-fluid system. *J. Fluid Mech.* **112**, 225–251.

LAMB, H. 1932 *Hydrodynamics*. Cambridge University Press.


https://doi.org/10.1017/jfm.2014.144 Published online by Cambridge University Press

LEIGHTON, F., BORTHWICK, A. & TAYLOR, P. 2010 1-D numerical modelling of shallow flows with variable horizontal density. *Intl J. Numer. Meth. Fluids* **62**, 1209–1231.

LEWIS, J. E., LAKE, B. M. & KO, D. R. S. 1974 On the interaction of internal waves and surface gravity waves. *J. Fluid Mech.* **64**, 773–800.

LIU, C.-M. 2006 Second-order random internal and surface waves in a two-fluid system. *Geophys. Res. Lett.* **33**, L06610.

LIU, P. L.-F. & WANG, X. 2012 A multilayer model for nonlinear internal wave propagation in shallow water. *J. Fluid Mech.* **695**, 341–365.

LO, J.-M. 1991 Air bubble barrier effect on neutrally buoyant objects. *J. Hydraul Res.* **29** (4), 437–455.

LONGUET-HIGGINS, M. S. & STEWART, R. W. 1960 Changes in the form of short gravity waves on long waves and tidal currents. *J. Fluid Mech.* **8**, 565–583.

LOWE, R. J., ROTTMAN, J. W. & LINDEN, P. F. 2005 The non-Boussinesq lock-exchange problem. Part 1. Theory and experiments. *J. Fluid Mech.* **537**, 101–124.

LYNETT, P. & LIU, P. L.-F. 2002*a* A numerical study of submarine landslide generated waves and runup. *Proc. R. Soc. Lond.* A **458**, 2885–2910.

LYNETT, P. & LIU, P. L.-F. 2002*b* A two-dimensional, depth-integrated model for internal wave propagation. *Wave Motion* **36**, 221–240.

LYNETT, P. & LIU, P. L.-F. 2004 A two-layer approach to wave modelling. *Proc. R. Soc. Lond.* A **460**, 2637–2669.

MA, Y.-C. 1982 Effect of long waves on the evolution of deep-water surface gravity waves. *Phys. Fluids* **25** (3), 411–419.

MA, G., SHI, F. & KIRBY, J. T. 2011 A polydisperse two-fluid model for surf zone bubble simulation. *J. Geophys. Res.* **116**, C05010.

MELLOR, G. L. 1991 An equation of state for numerical models of oceans and estuaries. *J. Atmos. Ocean. Technol.* **8**, 609–611.

MILGRAM, J. H. 1983 Mean flow in round bubble plumes. *J. Fluid Mech.* **133**, 345–376.

NGUYEN, H. Y. & DIAS, F. 2008 A Boussinesq system for two-way propagation of interfacial waves. *Physica* D **237**, 2365–2389.

NWOGU, O. 1993 Alternative form of Boussinesq equations for nearshore wave propagation. *ASCE J. Waterway Port Coastal Ocean Engng* **119** (6), 618–638.

PĂRĂU, E. & DIAS, F. 2001 Interfacial periodic waves of permanent form with free-surface boundary conditions. *J. Fluid Mech.* **437**, 325–336.

PHILLIPS, O. M. 1977 *Dynamics of the Upper Ocean*. 2nd edn. Cambridge University Press.

SCHÄFFER, H. A. 1996 Second-order wavemaker theory for irregular waves. *Ocean Engng* **23** (1), 47–88.

SEGUR, H. & HAMMACK, J. L. 1982 Soliton models of long internal waves. *J. Fluid Mech.* **118**, 285–305.

SELEZOV, I. T., AVRAMEKO, O. V., GURTOVYI, Y. V. & NARADOVYI, V. V. 2010 Nonlinear interaction of internal and surface gravity waves in a two-layer fluid with free surface. *J. Math. Sci.* **168** (4), 590–602.

SHARMA, J. N. & DEAN, R. G. 1981 Second-order directional seas and associated wave forces. *Soc. Petrol. Engng J.* **4**, 129–140.

SON, S. & LYNETT, P. 2014 Interaction of dispersive water waves with weakly sheared currents of arbitrary profile. *Coast. Engng* (submitted).

STRAUB, L. G., BOWERS, C. E. & TARAPORE, Z. S. 1959 *Experimental studies of pneumatic and hydraulic breakwaters.* Technical Paper No. 25, Series B, St. Anthony Falls Hydraulic Laboratory, University of Minnesota, Minneapolis, USA.

TAYLOR, G. 1955 The action of a surface current used as a breakwater. *Proc. R. Soc. Lond.* A **231**, 446–478.

TORO, E. F. 2002 *Shock-Capturing Methods for Free-Surface Shallow Flows*. Wiley.

UMEYAMA, M. 2002 Experimental and theoretical analyses of internal waves of finite amplitude. *ASCE J. Waterway Port Coastal Ocean Engng* **128** (3), 133–141.

WEI, G., KIRBY, J. T., GRILLI, S. T. & SUBRAMANYA, R. 1995 A fully nonlinear Boussinesq model for surface waves. I. Highly nonlinear unsteady waves. *J. Fluid Mech.* **294**, 71–92.

https://doi.org/10.1017/jfm.2014.144 Published online by Cambridge University Press

WOOD, I. R. 1970 A lock exchange flow. *J. Fluid Mech.* **42**, 671–687.

YAMAMOTO, S. & DAIGUJI, H. 1993 Higher-order-accurate upwind schemes for solving the compressible Euler and Navier–Stokes equations. *Comput. Fluids* **22**, 259–270.

ZHANG, C.-X., WANG, Y.-X., WANG, G.-Y. & YU, L.-M. 2010 Wave dissipating performance of air bubble breakwaters with different layouts. *J. Hydrodyn.* B **22** (5), 671–680.

ZHOU, J. G., CAUSON, D. M., MINGHAM, C. G. & INGRAM, D. M. 2001 The surface gradient method for the treatment of source terms in the shallow water equations. *J. Comput. Phys.* **168** (2), 1–25.

https://doi.org/10.1017/jfm.2014.144 Published online by Cambridge University Press